



A van der Waals pn heterojunction with organic/inorganic semiconductors

Cite as: Appl. Phys. Lett. **107**, 183103 (2015); <https://doi.org/10.1063/1.4935028>

Submitted: 04 August 2015 . Accepted: 09 October 2015 . Published Online: 02 November 2015

Daowei He , Yiming Pan, Haiyan Nan, Shuai Gu, Ziyi Yang, Bing Wu , Xiaoguang Luo, Bingchen Xu, Yuhan Zhang, Yun Li, Zhenhua Ni, Baigeng Wang, Jia Zhu, Yang Chai, Yi Shi, and Xinran Wang



View Online



Export Citation



CrossMark

ARTICLES YOU MAY BE INTERESTED IN

[Heterostructures based on inorganic and organic van der Waals systems](#)

APL Materials **2**, 092511 (2014); <https://doi.org/10.1063/1.4894435>

[Band offsets and heterostructures of two-dimensional semiconductors](#)

Applied Physics Letters **102**, 012111 (2013); <https://doi.org/10.1063/1.4774090>

[Hopping and band mobilities of pentacene, rubrene, and 2,7-dioctyl\[1\]benzothieno\[3,2-b\]\[1\]benzothiophene \(C₈-BTBT\) from first principle calculations](#)

The Journal of Chemical Physics **139**, 014707 (2013); <https://doi.org/10.1063/1.4812389>

Lock-in Amplifiers

Find out more today



 Zurich Instruments

A van der Waals pn heterojunction with organic/inorganic semiconductors

Daowei He,^{1,a)} Yiming Pan,^{2,a)} Haiyan Nan,³ Shuai Gu,⁴ Ziyi Yang,¹ Bing Wu,¹ Xiaoguang Luo,³ Bingchen Xu,¹ Yuhan Zhang,¹ Yun Li,¹ Zhenhua Ni,³ Baigeng Wang,² Jia Zhu,⁴ Yang Chai,⁵ Yi Shi,^{1,b)} and Xinran Wang^{1,b)}

¹National Laboratory of Solid State Microstructures, School of Electronic Science and Engineering, and Collaborative Innovation Center of Advanced Microstructures, Nanjing University, Nanjing 210093, China

²National Laboratory of Solid State Microstructures, School of Physics, Nanjing University, Nanjing 210093, China

³Department of Physics, Southeast University, Nanjing 211189, China

⁴College of Engineering and Applied Science, Nanjing University, Nanjing 210093, China

⁵Department of Applied Physics, The Hong Kong Polytechnic University, Hung Hom, Kowloon, Hong Kong

(Received 4 August 2015; accepted 9 October 2015; published online 2 November 2015)

van der Waals (vdW) heterojunctions formed by two-dimensional (2D) materials have attracted tremendous attention due to their excellent electrical/optical properties and device applications. However, current 2D heterojunctions are largely limited to atomic crystals, and hybrid organic/inorganic structures are rarely explored. Here, we fabricate the hybrid 2D heterostructures with p-type dioctylbenzothienobenzothiophene (C₈-BTBT) and n-type MoS₂. We find that few-layer C₈-BTBT molecular crystals can be grown on monolayer MoS₂ by vdW epitaxy, with pristine interface and controllable thickness down to monolayer. The operation of the C₈-BTBT/MoS₂ vertical heterojunction devices is highly tunable by bias and gate voltages between three different regimes: interfacial recombination, tunneling, and blocking. The pn junction shows diode-like behavior with rectifying ratio up to 10⁵ at the room temperature. Our devices also exhibit photovoltaic responses with a power conversion efficiency of 0.31% and a photoresponsivity of 22 mA/W. With wide material combinations, such hybrid 2D structures will offer possibilities for opto-electronic devices that are not possible from individual constituents.

© 2015 AIP Publishing LLC. [<http://dx.doi.org/10.1063/1.4935028>]

Heterojunctions are the essential building blocks of modern semiconductor devices such as light-emitting diodes and solid-state lasers.^{1,2} With the discovery of graphene and other two-dimensional (2D) materials,^{3–5} van der Waals (vdW) heterojunctions have recently created many attractive opportunities. Unlike the traditional heterojunctions grown by molecular beam epitaxy, vdW heterojunctions do not require lattice match at the interface, allowing virtually unlimited materials combination. Prototype devices, such as tunneling transistors,⁶ photodetectors,⁷ light-emitting diodes,^{8,9} and photovoltaic devices,¹⁰ have been demonstrated. So far, most of the vdW heterostructures are fabricated by mechanical transfer of 2D layered atomic crystals.⁵ Although this method could demonstrate proof-of-concept devices, it cannot be scaled up for real applications. In addition, it is difficult to precisely control the stacking orientation of the heterojunction,¹¹ which may cause significant variations of device performance.¹²

As an alternative to layered atomic crystals, 2D molecular crystals including oligomers¹³ and polymers^{14,15} have recently emerged as an interesting class of materials. Particularly, the recent demonstration of vdW epitaxial growth of 2D molecular crystal on graphene suggests the possibility of organic/inorganic hybrid structures.^{13,16,17} The epitaxial process offers advantages of low temperature, atomically smooth and clean interface, accurate control of

morphology, and the ability to scale up.^{13,16–21} The hybrid heterojunctions will further benefit from a much larger library of organic semiconductor materials²² that allow more design freedom of the devices. So far, however, only limited attempt has been made to interface transition-metal dichalcogenides (TMDs), the most important class of 2D atomic semiconductors, with molecular semiconductors.²³

In this work, we demonstrated the epitaxial growth of few-layer p-type dioctylbenzothienobenzothiophene (C₈-BTBT) molecular crystals on n-type MoS₂ and systematically studied the electrical transport and photovoltaic responses of the heterojunction. At room temperature, the pn junction device showed a rectifying ratio up to 10⁵. Under forward bias, the device was operated by either interfacial recombination or tunneling, depending on the backgate voltage. The operation mechanism of the heterojunction device was consistent with the band structure analysis and the variable-temperature electrical measurements. We also observe strong photovoltaic effects in the heterojunction devices. Our study shows that 2D organic/inorganic vdW heterojunctions may be used for the future electronic and optoelectronic device applications.

Recently, we demonstrated the epitaxial growth of highly ordered, few-layer C₈-BTBT crystals on graphene and BN. Here, we adopted similar methods but with the mechanically exfoliated MoS₂ as the epitaxy substrate (see experimental section of the supplementary material²⁴). Monolayer MoS₂ was exfoliated from bulk flakes on 285 nm SiO₂/Si without thermal annealing and identified by atomic force microscope

^{a)}D. He and Y. Pan contributed equally to this work.

^{b)}Authors to whom correspondence should be addressed. Electronic addresses: yshi@nju.edu.cn and xrwang@nju.edu.cn.

(AFM) and Raman spectroscopy (Figures 1(b) and 1(d)). Figures 1(b) and 1(c) show the AFM images of the same MoS₂ before and after growth, with up to three layers of C₈-BTBT grown atop. The C₈-BTBT crystals were also confirmed by Raman spectroscopy with two characteristic peaks near 1470 cm⁻¹ and 1550 cm⁻¹ (Figure 1(d)).¹³ The growth of C₈-BTBT molecular crystals proceeded in a layer-by-layer fashion similar to that on graphene substrate. However, we also observed several interesting distinctions. (1) The thickness of the first C₈-BTBT layer (1L) and subsequent layers were ~1.4 nm and ~2.9 nm, respectively (Figures 1(e) and S1). This is very different from the growth on graphene, where an additional interfacial layer with a thickness ~0.6 nm existed because of the strong molecule-substrate vdW interactions.¹³ Since MoS₂ is not a π -conjugated system and the lattice constants are quite different from graphene, the vdW forces between C₈-BTBT molecules and MoS₂ are significantly reduced and comparable to the inter-molecular interactions. The competition between these forces thus led to the titled molecular packing shown in Figure 1(a).^{13,16,17} The subsequent layers above 1L were dominated by inter-molecular interactions, giving a bulk-like molecular packing²⁵ with a layer thickness of ~2.9 nm. (2) We observed a higher density of nucleation sites forming on MoS₂ than on graphene, especially at the edges (Figure S2). Since the nucleation of C₈-BTBT occurs preferably at places with high surface energy,¹³ we speculate that the high nucleation density may result from surface defects of MoS₂. Indeed, many studies have shown that high density of sulfur vacancies, among other defects, exist in MoS₂.^{26,27} However, the high nucleation density does not appear to significantly affect the vertical charge transport as shown below.

With the C₈-BTBT/MoS₂ heterostructures, we fabricated vertical field-effect transistors (Figure 2(a)) and study the electrical transport properties (see Figure S3 for detailed device fabrication procedure²⁴). Figure 2(c) shows the room-temperature current density ($J_{ds} = I_{ds}/A$, where I_{ds} is the

source-drain current and A is the area of the heterojunction) as a function of backgate voltage V_g for a representative device ($V_{ds} = 1, 5, \text{ and } 9 \text{ V}$, respectively). Interestingly, the transfer characteristics were very different from the conventional planar FETs with either MoS₂ or C₈-BTBT channel (Figure S4). At negative V_g , J_{ds} showed a clear peak at low biases. With the increase of V_g , J_{ds} abruptly jumped up and becomes roughly independent of V_g . However, the conductance in this regime was strongly modulated by V_{ds} .

The two regimes in the transfer characteristics suggest different transport mechanisms. In order to understand the operation mechanism, we draw the band diagram of the heterojunction device under forward bias as shown in Figure 2(b). Considering that C₈-BTBT is a wide bandgap (~3.8 eV) semiconductor with the highest occupied molecular orbit of 5.39 eV and lowest unoccupied molecular orbit of 1.55 eV (Ref. 28) and that the edge of conduction band (E_{CB}) and valance band (E_{VB}) of monolayer MoS₂ are 4.3 eV and 5.9 eV,²⁹ the heterojunction is of type II with a staggered gap. Since C₈-BTBT and MoS₂ are p-type and n-type semiconductors as determined by the semiconductor/metal contact, there is only a narrow range in V_g where both materials conduct (Figure S4). Within this range, electrons and holes are able to inject from the Schottky barriers (SBs) at Au/MoS₂ and Au/C₈-BTBT, respectively, by the thermionic emission (TE) and recombine at the interface (Figure 2(b), left panel). Since the conductance in this regime is limited by the minority carrier, a peak in the transfer characteristics is expected (Figure S4). Therefore, we attribute the peak under negative V_g to interfacial recombination regime.

As V_g was further increased beyond the recombination regime, the injection of holes from C₈-BTBT was completely blocked, while electrons could still be injected from MoS₂. This resulted in strong accumulation of electrons in MoS₂ (Figure 2(b), middle panel). Since the large energy barrier at the C₈-BTBT/MoS₂ interface blocked the thermal activation, the electron transport could only occur via tunneling in this

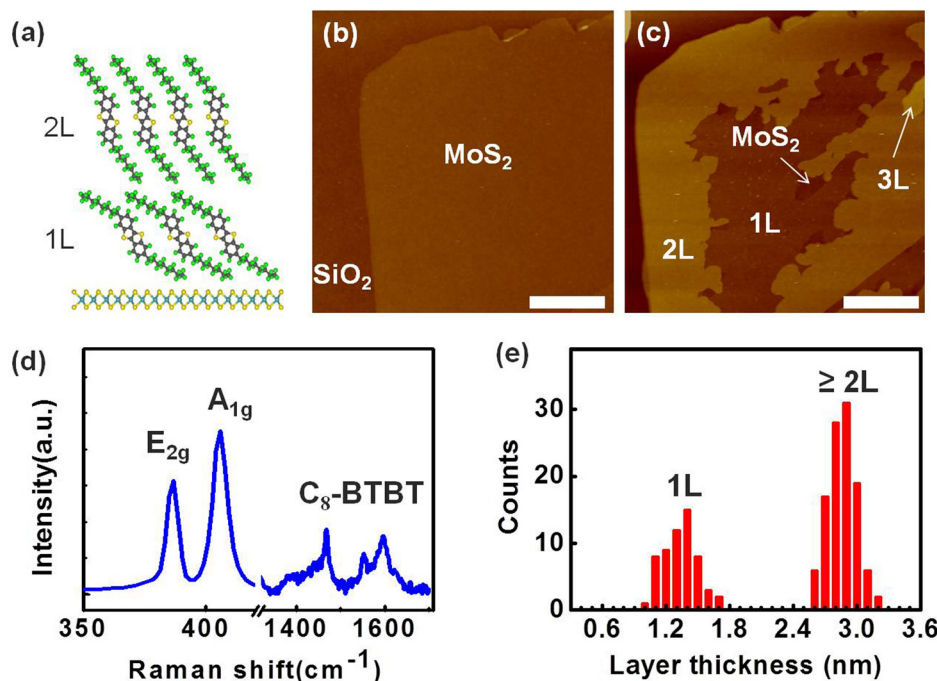


FIG. 1. (a) A schematic illustration of molecular packing of C₈-BTBT on MoS₂. (b) and (c) AFM snapshots of MoS₂ before and after the growth of C₈-BTBT molecular crystal. Scale bars: 1 μm . (d) Raman spectrum of C₈-BTBT grown on MoS₂. The E_{2g} and A_{1g} peaks are from MoS₂, and the other two peaks near 1470 cm⁻¹ and 1550 cm⁻¹ are from C₈-BTBT. (e) Histogram of the layer thickness of C₈-BTBT molecular crystals on MoS₂, from over 5 samples.

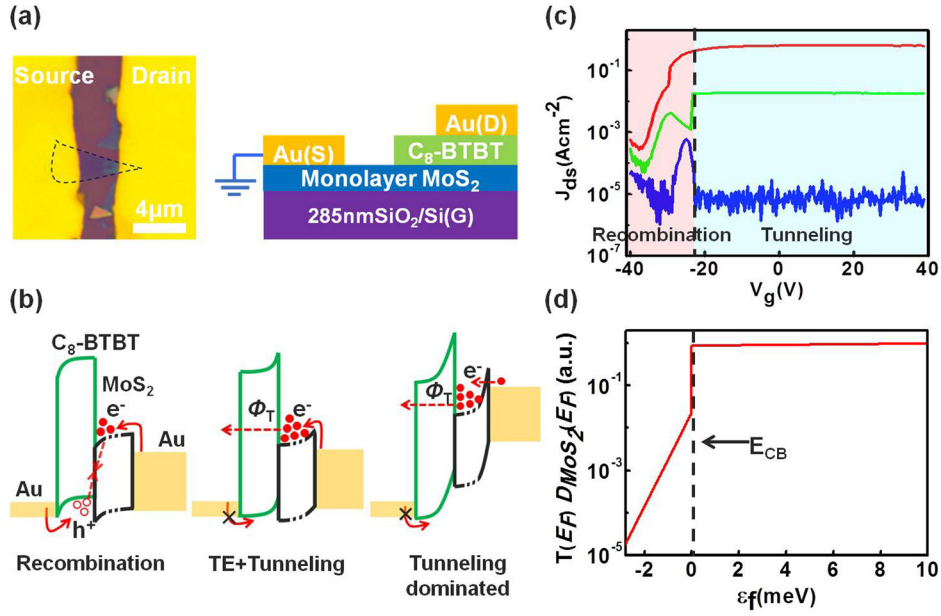


FIG. 2. (a) Left: microscope image of a vertical heterojunction device. The dotted line represents the shape of the monolayer MoS₂. The source and drain electrode is in contact with MoS₂ and C₈-BTBT, respectively. The multi-layer C₈-BTBT can be observed near the edge of the drain electrode. Right: schematic illustration of the device. (b) The band diagram of MoS₂/C₈-BTBT vertical heterojunction device under forward bias, showing different operation regimes. The dotted line is used to represent the lateral part of MoS₂. (c) Room-temperature J_{ds} - V_g characteristics of a typical MoS₂/C₈-BTBT vertical heterojunction device, $V_{ds} = 1$ V (blue line), 5 V (green line), and 9 V (red line). (d) The calculated $T(E_F)D_{MoS_2}(E_F)$ as a function of E_F in the tunneling regime. During the calculation, we used the following parameters: $D_T = 10^{13} \text{ eV}^{-1} \text{ cm}^{-2}$ and $\Delta = 14 \text{ meV}$. The dashed vertical line represents the conduction band edge of MoS₂.

regime. In order to understand the small modulation of tunneling current by V_g , we modeled the device as a single-barrier tunnel junction, that is, the barrier at C₈-BTBT/MoS₂ interface. Under constant V_{ds} , the tunneling current is approximately proportional to⁶

$$I_T \propto T(E_F)D_{MoS_2}(E_F), \quad (1)$$

where $T(E_F) = \exp\left(-\frac{2d}{\hbar}\sqrt{2m^* (U - E_F)}\right)$ is the transmission coefficient through the C₈-BTBT layer, E_F is the Fermi energy, $U = 2.75 \text{ eV}$ is the height of the tunnel barrier, m^* is the effective mass, $d = 16 \text{ nm}$ is the thickness of C₈-BTBT layers, and $D_{MoS_2}(E_F)$ is the density of states (DOS) of MoS₂ at the Fermi energy. D_{MoS_2} can be modeled as¹⁸

$$D_{MoS_2}(E) = \begin{cases} D_0, & E - E_{CB} \geq 0 \\ D_T \exp\left(\frac{E - E_{CB}}{\Delta}\right), & E - E_{CB} < 0, \end{cases} \quad (2)$$

where $D_0 = 3.8 \times 10^{14} \text{ eV}^{-1} \text{ cm}^{-2}$ is the DOS in the conduction band of MoS₂. The DOS in the conduction band is a constant because of the 2D nature of MoS₂. Below the band edge, the DOS has an exponential tail due to disorders and traps.^{18,27}

As V_g is swept from negative to positive, E_F of MoS₂ is increased proportionally but with very small magnitude because of the large DOS in MoS₂. In fact, for a gate overdrive of 40 V, E_F only increases by 7.6 meV, almost negligible compared U . Such small change of E_F (and therefore, transmission coefficient) qualitatively explains the small modulation of tunneling current by V_g as observed experimentally (Figure 2(c)). Indeed, the calculated $T(E_F)D_{MoS_2}(E_F)$ using Equations (1) and (2) clearly captures this feature (Figure 2(d)). The drop of current below the conduction band edge is due to the decay of DOS in the tail states.

Figure 3(a) plots the output characteristics under $V_g = 30 \text{ V}$, which shows an excellent rectifying behavior as expected for a pn junction. The room-temperature rectifying ratio could reach $\sim 1 \times 10^5$ (Figure S5b). Under reverse bias, the device showed a blocking behavior with little current flowing because of the increasing SB at both contacts to prevent carrier injection (Figure 3(a), inset). Under forward bias, however, we found that the current increased exponentially with V_{ds} under small bias ($V_{ds} < 4 \text{ V}$, Figure S5a) but less dramatically under large bias ($V_{ds} > 6 \text{ V}$). The much weaker current dependence under large bias was due to tunneling dominated process. This was also clear from the band diagram where the SB at the Au/MoS₂ contact became thin enough for electrons to tunnel through (Figure 2(b), right panel). Under small forward bias, the electron transport at the Au/MoS₂ Schottky junction was mainly through TE (Figure 2(b), middle panel), leading to the exponential dependence on V_{ds} . In this regime, the output current of the heterojunction device can be calculated as

$$I_{tot} \propto T(V_g) \times I_{TE} = I_0 \left(\exp\left(\frac{eV_{ds}}{\eta k_B T}\right) - 1 \right), \quad (3)$$

where $T(V_g)$ is the tunneling transmission coefficient through C₈-BTBT, η is the ideality factor considering the fact that V_{ds} does not fully drop on the Schottky junction

$$I_0 = T(V_g) A A^* T^2 e^{-e\Phi_{SB}/k_B T} \quad (4)$$

is the reverse saturation current, A is the area of the Schottky junction, A^* is the effective Richardson constant, and Φ_{SB} is the SB height for electrons at the Au/MoS₂ contact. From variable-temperature measurements, we were able to extract Φ_{SB} , which is an important device parameter. Figure 3(b)

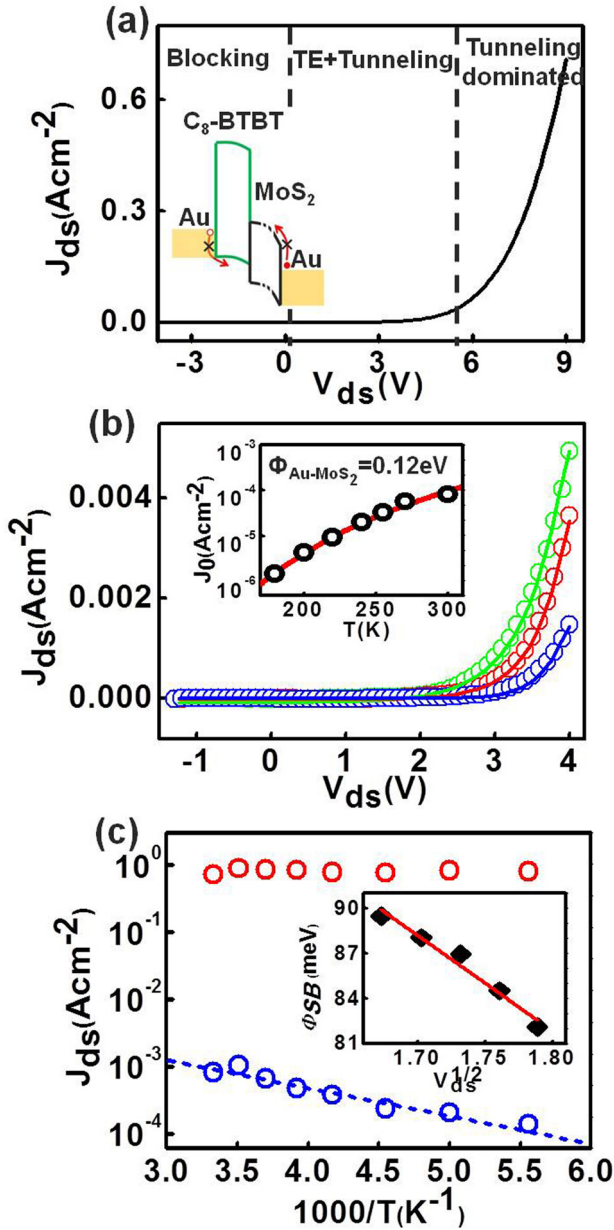


FIG. 3. (a) Room-temperature J_{ds} - V_{ds} characteristics of same device in Figure 2 under $V_g = 30$ V. The different operation regimes are separated by vertical dashed lines. Inset shows the band diagram under reverse bias. (b) J_{ds} - V_{ds} characteristics of same device in (a) under $V_g = 30$ V at $T = 300$ K (red symbols), 240 K (green symbols), and 180 K (blue symbols). Lines are the fitting results using Eq. (2). Inset: the reverse saturation current density J_0 as a function of temperature (black symbols) and theoretical fitting using Eq. (4) (red line). $\Phi_{SB} = 0.12$ eV is derived for the Au/MoS₂ interface. (c) Arrhenius plot of J_{ds} of the same device in (a) under $V_g = 30$ V. Red symbol: $V_{ds} = 9$ V and blue symbol: $V_{ds} = 3$ V. The blue dashed line is the linear fitting of the Arrhenius plot. The extracted Φ_{Au-MoS_2} are plotted in the inset as a function of $V_{ds}^{1/2}$ (black square). The extrapolated Φ_{Au-MoS_2} at zero bias is 0.19 eV (red line).

shows the output characteristics under 180 K, 240 K, and 300 K, respectively. We could fit all the output characteristics with the same ideality factor $\eta = 20.6$ (Figure S6) and extract the reverse saturation current $J_0 = I_0/A$ as a function of temperature (Figure 3(b) inset, symbols). The J_0 - T relationship is well described by Eq. (4) with $\Phi_{SB} = 120$ meV (Figure 3(b) inset, line). The extracted Φ_{SB} is consistent with the widely observed n-type behavior in Au-contacted MoS₂ transistors.³⁰ The small SB for electrons suggests strong

Fermi level pinning at the Au/MoS₂ interface,^{31,32} likely dominated by defects and interfacial traps in MoS₂.

We were also able to corroborate the proposed device model by the low temperature measurements. Figure 3(c) is the Arrhenius plot of current density under two different regimes. For $V_{ds} > 6$ V, we observed that the conductance was insensitive to temperature, a strong evidence for tunneling-dominated current. However, for $V_{ds} < 4$ V, the conductance showed an exponential relationship with temperature, consistent with TE. From the linear fitting of the Arrhenius plot (Figure 3(c), blue dashed line), Φ_{SB} was extracted and found to scale linearly with $V_{ds}^{1/2}$, due to the image force as in conventional Schottky junctions.² The extrapolated $\Phi_{SB} = 190$ meV at zero bias (Figure 3(c) inset) is in a good agreement with the fitting in Figure 3, reassuring the consistency of our theoretical model.

We further investigated the photo-response of our devices. To this end, we carried out photovoltaic measurements under the white light illumination from a standard solar simulator with incident optical power P_{opt} varying between 100 and 1100 W/m² in ambient condition. Figure 4 shows clear photovoltaic effect of a representative device with 8-layer C₈-BTBT crystals. The open circuit voltage V_{oc} is about 0.5 V. The power conversion efficiency, defined as $\eta = P_{el,m}/P_{opt}$, is up to 0.31%, which is comparable to values reported for lateral monolayer WSe₂ pn junctions.³³ The photoresponsibility $R = I_{ds}/P_{opt}$ under zero V_{ds} is ~ 22 mA/W. We make it clear that the power conversion efficiency is estimated using the exposed area of the heterojunction, rather than the area covered by Au. We also note that the efficiency is just a rough estimate. We believe that much better performances are possible with further device optimization (e.g., transparent top electrodes). The photo-response should be a general feature of the hybrid heterojunction. With many possible combinations of TMDs and organic materials, we expect this type of devices could be very versatile and useful in photovoltaic or photodetector applications.

In conclusion, we have demonstrated that high-quality few-layer molecular semiconductors can be epitaxially grown on TMDs, creating a 2D hybrid organic/inorganic

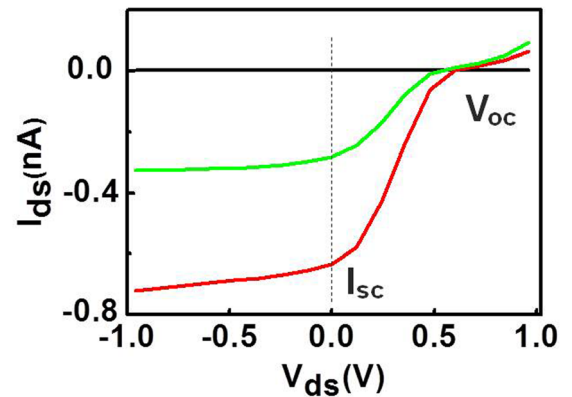


FIG. 4. I_{ds} - V_{ds} characteristics of a heterojunction device under white light illumination with $P_{opt} = 1100$ W/m² (red), 550 W/m² (green), and under dark condition (black). The measurements were taken at $V_g = -30$ V under ambient condition. V_{oc} and I_{sc} present open circuit voltage and short circuit current, respectively.

vdW heterojunction. In a vertical heterojunction device created by p-type C₈-BTBT and n-type MoS₂, we observed an excellent rectifying behavior as well as strong photovoltaic responses. Considering the huge library of organic semiconductors, our work opens up many design possibilities for 2D heterostructure devices.

We thank NIPPON KAYAKU Co., Ltd., Japan, for providing C₈-BTBT materials. This work was supported in part by the National Key Basic Research Program of China (2013CBA01604 and 2015CB921600); the National Natural Science Foundation of China (61325020, 61261160499, 11274154, 61521001, and 61574074); the MICM Laboratory Foundation (9140C140105140C14070); a project funded by the Priority Academic Program Development of Jiangsu Higher Education Institutions; “Jiangsu Shuangchuang” program; and “Jiangsu Shuangchuang Team” Program.

- ¹H. Kroemer, *Proc. IEEE* **70**, 13 (1982).
- ²S. M. Sze and K. K. Ng, *Physics of Semiconductor Devices* (Wiley, Hoboken, NJ, USA, 2006).
- ³K. S. Novoselov and A. K. Geim, *Nat. Mater.* **6**, 183 (2007).
- ⁴Q. Wang, K. Kalantar-Zadeh, A. Kis, J. N. Coleman, and M. S. Strano, *Nat. Nanotechnol.* **7**, 699 (2012).
- ⁵A. K. Geim and I. V. Grigorieva, *Nature* **499**, 419 (2013).
- ⁶L. Britnell, R. V. Gorbachev, R. Jalil, B. D. Belle, F. Schedin, A. Mishchenko, T. Georgiou, M. I. Katsnelson, L. Eaves, S. V. Morozov, N. M. R. Peres, J. Leist, A. K. Geim, K. S. Novoselov, and L. A. Ponomarenko, *Science* **335**, 947 (2012).
- ⁷W. J. Yu, Y. Liu, H. Zhou, A. Yin, Z. Li, Y. Huang, and X. Duan, *Nat. Nanotechnol.* **8**, 952 (2013).
- ⁸J. S. Ross, P. Klement, A. M. Jones, N. J. Ghimire, J. Yan, D. G. Mandrus, T. Taniguchi, K. Watanabe, K. Kitamura, W. Yao, D. H. Cobden, and X. Xu, *Nat. Nanotechnol.* **9**, 268 (2014).
- ⁹F. Withers, O. Del Pozo-Zamudio, A. Mishchenko, A. P. Rooney, A. Gholinia, K. Watanabe, T. Taniguchi, S. J. Haigh, A. K. Geim, A. I. Tartakovskii, and K. S. Novoselov, *Nat. Mater.* **14**, 301 (2015).
- ¹⁰M. M. Furchi, A. Pospischil, F. Libisch, J. Burgdörfer, and T. Mueller, *Nano Lett.* **14**(8), 4785 (2014).
- ¹¹W. Yang, G. Chen, Z. Shi, C. Liu, L. Zhang, G. Xie, M. Cheng, D. Wang, R. Yang, D. Shi, K. Watanabe, T. Taniguchi, Y. Yao, Y. Zhang, and G. Zhang, *Nat. Mater.* **12**, 792 (2013).
- ¹²B. Fallahazad, K. Lee, S. Kang, J. Xue, S. Larentis, C. Corbet, K. Kim, H. C. P. Movva, T. Taniguchi, K. Watanabe, L. F. Register, S. K. Banerjee, and E. Tutuc, *Nano Lett.* **15**(1), 428 (2015).
- ¹³D. He, Y. Zhang, Q. Wu, R. Xu, H. Nan, J. Liu, J. Yao, Y. Li, Y. Shi, J. Wang, L. He, Z. Ni, F. Miao, F. Song, H. Xu, K. Watanabe, T. Taniguchi, J. Xu, and X. Wang, *Nat. Commun.* **5**, 5162 (2014).
- ¹⁴M. J. Kory, M. Wörle, T. Weber, P. Payamyar, S. W. van de Poll, J. Dshemuchadse, N. Trapp, and A. D. Schlüter, *Nat. Chem.* **6**, 779 (2014).
- ¹⁵P. Kissel, D. J. Murray, W. J. Wulfstange, V. J. Catalano, and B. T. King, *Nat. Chem.* **6**, 774 (2014).
- ¹⁶K. Kim, T. H. Lee, E. J. G. Santos, P. S. Jo, A. Salleo, Y. Nishi, and Z. Bao, *ACS Nano* **9**, 5922 (2015).
- ¹⁷K. Kim, E. J. G. Santos, T. H. Lee, Y. Nishi, and Z. Bao, *Small* **11**(17), 2037 (2015).
- ¹⁸C. R. Dean, A. F. Young, I. Meric, C. Lee, L. Wang, S. Sorgenfrei, K. Watanabe, T. Taniguchi, P. Kim, K. L. Shepard, and J. Hone, *Nat. Nanotechnol.* **5**, 722 (2010).
- ¹⁹C. Lee, T. Schiros, E. J. G. Santos, B. Kim, K. G. Yager, S. J. Kang, S. Lee, J. Yu, K. Watanabe, T. Taniguchi, J. Hone, E. Kaxiras, C. Nuckolls, and P. Kim, *Adv. Mater.* **26**, 2812 (2014).
- ²⁰H. Hlaing, C. Kim, F. Carta, C. Nam, R. A. Barton, N. Petrone, J. Hone, and I. Kymissis, *Nano Lett.* **15**, 69 (2015).
- ²¹S. Parui, L. Pietrobon, D. Ciudad, S. Vélez, X. Sun, F. Casanova, P. Stoliar, and L. E. Hueso, *Adv. Funct. Mater.* **25**, 2972 (2015).
- ²²C. Wang, H. Dong, W. Hu, Y. Liu, and D. Zhu, *Chem. Rev.* **112**, 2208 (2012).
- ²³F. Liu, W. L. Chow, X. He, P. Hu, S. Zheng, X. Wang, J. Zhou, Q. Fu, W. Fu, P. Yu, Q. Zeng, H. Fan, B. K. Tay, C. Kloc, and Z. Liu, *Adv. Funct. Mater.* **25**(36), 5865–5871 (2015).
- ²⁴See supplementary material at <http://dx.doi.org/10.1063/1.4935028> for experimental methods and additional device data.
- ²⁵H. Minemawari, T. Yamada, H. Matsui, J. Tsutsumi, S. Haas, R. Chiba, R. Kumai, and T. Hasegawa, *Nature* **475**(21), 364 (2011).
- ²⁶J. Hong, Z. Hu, M. Probert, K. Li, D. Lv, X. Yang, L. Gu, N. Mao, Q. Feng, L. Xie, J. Zhang, D. Wu, Z. Zhang, C. Jin, W. Ji, X. Zhang, J. Yuan, and Z. Zhang, *Nat. Commun.* **6**, 6293 (2015).
- ²⁷Z. Yu, Y. Pan, Y. Shen, Z. Wang, Z.-Y. Ong, T. Xu, R. Xin, L. Pan, B. Wang, L. Sun, J. Wang, G. Zhang, Y. W. Zhang, Y. Shi, and X. Wang, *Nat. Commun.* **5**, 5290 (2014).
- ²⁸H. Kobayashi, N. Kobayashi, S. Hosoi, N. Koshitani, D. Murakami, R. Shirasawa, Y. Kudo, D. Hobara, Y. Tokita, and M. Itabashi, *J. Chem. Phys.* **139**, 014707 (2013).
- ²⁹J. Kang, S. Tongay, J. Zhou, J. Li, and J. Wu, *Appl. Phys. Lett.* **102**, 012111 (2013).
- ³⁰B. Radisavljevic, A. Radenovic, J. Brivio, V. Giacometti, and A. Kis, *Nat. Nanotechnol.* **6**, 147 (2011).
- ³¹C. Gong, L. Colombo, R. M. Wallace, and K. Cho, *Nano Lett.* **14**, 1714 (2014).
- ³²W. Chen, E. J. G. Santos, W. Zhu, E. Kaxiras, and Z. Zhang, *Nano Lett.* **13**, 509 (2013).
- ³³A. Pospischil, M. M. Furchi, and T. Mueller, *Nat. Nanotechnol.* **9**, 257 (2014).